Materials Horizons

ROYAL SOCIETY OF CHEMISTRY

COMMUNICATION

View Article Online
View Journal

Cite this: DOI: 10.1039/d5mh01409c

Received 6th August 2025,
Accepted 5th November 2025

DOI: 10.1039/d5mh01409c

rsc.li/materials-horizons

Power-tunable multicolor upconversion in nanocrystals under single-wavelength excitation

Raheel Ahmed Janjua,†[ab] Li Xu,†[cd] Xinyu Wang,[d] Joan J. Carvajal,[e] Ruili Zhang,[a] Lu Liu *[cd] and Sailing He *[abfg]

In this work, we demonstrate for the first time tunable upconversion luminescence in three primary colors using a single excitation wavelength of 980 nm, *via* altering the excitation intensity. A core/shell/shell nanocrystal of about 50 nm diameter was synthesized using a design strategy with 2% Er^{3+} and 98% Yb^{3+} in the core, and the outer shell is made of $NaYF_4$:Yb^{3+},Tm^{3+} (with 2% Tm^{3+} and 18% Yb^{3+}), separated by an inert intermediate shell. This rationally designed architecture enables green, red, and blue light emissions by modulating the excitation power density, leveraging the photon-order-dependent upconversion process. As the power density of the 980 nm continuous-wave (CW) laser increases, the emission color shifts systematically from green to red and ultimately to blue, corresponding to the involvement of 2-photon, 3-photon, and 4-photon processes, respectively. Chromaticity coordinate shifts on the CIE diagram validated this dynamic color modulation, demonstrating precise control over emission pathways. The findings offer a simplified yet highly versatile excitation setup for full RGB tunability, paving the way for advancements in photonics and enabling possibilities in high-resolution color display and biomedical applications.

New concepts

We introduce a fundamentally new concept in upconversion photonics: full RGB color tunability in individual nanocrystals using continuous-wave (CW) excitation at a single wavelength (980 nm) through simple adjustment of excitation power density. This is achieved *via* a compact core/shell/shell architecture doped with Er^{3+}, Yb^{3+}, and Tm^{3+} ions, where rational spatial segregation enables sequential activation of 2-, 3-, and 4-photon processes, producing green, red, and blue emissions, respectively. In contrast to existing strategies that require complex multi-layer structures, pulsed excitation, time-gated detection, or multiple excitation wavelengths, our approach offers a structurally simple and scalable design with real-time power-tunable color output. This marks the first demonstration of full-spectrum (RGB) emission tunability in single nanocrystals under CW single-wavelength excitation without temporal modulation. This work offers new insight into photon-order engineering in lanthanide-doped nanomaterials, enabling deterministic color switching *via* nonlinear excitation pathways. The concept lays a foundation for pixel-level color programmability and miniaturized optical control, with implications for high-resolution display technologies, anti-counterfeiting and smart bio-imaging. It shifts the design paradigm from wavelength/time-domain multiplexing to excitation-power-based modulation in upconversion systems.

Introduction

Over the past decade, lanthanide ion (Ln^{3+})-doped nanocrystals with fixed compositions and tunable upconversion colors have attracted considerable attention due to their promising applications in 3D color display devices, information storage, and advanced anti-counterfeiting technologies.[1–5] Traditionally, color-tunable upconversion luminescence has been achieved by modifying sample compositions, such as adjusting dopant concentrations,[6] doping with different lanthanide ions,[7] introducing luminescent quenchers,[8] or varying the spacing of emitting ions in multilayered particles.[9] However, these strategies generally result in specific emission colors that may be suited to only certain applications. For instance, near-infrared (NIR) photons penetrate deeply into biological tissues,[10,11] red light within the biological window I (BW-I) is advantageous for visible imaging,[12,13] green light is particularly sensitive to

[a] Zhejiang Engineering Research Center for Intelligent Medical Imaging, Sensing and Non-invasive Rapid Testing, Taizhou Hospital, Zhejiang University, Taizhou, China
[b] Centre for Optical and Electromagnetic Research, National Engineering Research Center for Optical Instruments, College of Optical Science and Engineering, Zhejiang University, Hangzhou 310058, China
[c] Key Lab of In-fiber Integrated Optics, Ministry Education of China, Harbin Engineering University, Harbin 150001, P. R. China. E-mail: liulu@hrbeu.edu.cn
[d] School of Physics and Optoelectronics Engineering, Harbin Engineering University, Harbin 150001, P. R. China
[e] Departament Quimica Fisica i Inorganica, Campus Sescelades, Universitat Rovira i Virgili, Tarragona, E-43007, Spainelades
[f] Shanghai Institute for Advanced Study, Zhejiang University, Shanghai 201203, People's Republic of China
[g] Department of Electromagnetic Engineering, School of Electrical Engineering, Royal Institute of Technology, S-100 44 Stockholm, Sweden. E-mail: sailing@kth.se
† These two authors contributed equally.

human vision, and blue and ultraviolet (UV) lights are optimal for triggering photochemical reactions.[14] There is significant demand for luminescent materials that emit multiple colors in a tunable fashion.[15–20] Achieving tunable luminescence in upconversion nanocrystals with fixed ion compositions is challenging because these nanocrystals are minimally responsive to environmental changes. As a result, ambient temperature, moisture, electric field, or pressure variations generally induce only slight shifts in emission color.

Multi-wavelength excitation strategies have been widely employed as one of the most effective approaches for achieving color/spectral tunability in single particles. In this method, each wavelength stimulates distinct Ln^{3+} ions to emit different colors, enabling precise color tuning with high brightness and color purity. This is achieved by spatially combining different nanocrystals doped with distinct lanthanides through core–shell structural engineering. For instance, in 2016, Li *et al.* pioneered a dual-color approach in single nanocrystals,[21] achieving blue and green emissions under 980 nm and 796 nm excitations, respectively, using absorption filtration. Wu *et al.* demonstrated tunable blue (Ex = 980 nm) and red (Ex = 800 nm) emissions with a similar method using multiple wavelengths.[22] Lei *et al.* achieved tunable green and red emissions by manipulating energy migration *via* dual-excitation strategies,[23] and another group demonstrated tunable red/green emissions under 980/1530 nm excitation. Most recently, Hong *et al.* realized RGB emission using a highly complex seven-layer nanostructure under three excitation wavelengths (800, 980, and 1530 nm).[24] Although effective, these multi-wavelength strategies require multiple excitation sources, significantly increasing the optical complexity and cost of luminescence tunability setups.

Structural complexity in multi-shell nanocrystals has also been exploited to achieve color modulation. In these approaches, different shells are doped with specific activators and separated by inert layers to suppress cross-relaxation, thereby controlling competing energy transfer pathways. While this strategy is effective, it often requires 4 to 6 shells with finely optimized thickness and composition.[25] Such intricate designs are time-consuming to synthesize, costly, and difficult to reproduce at scale, which limits their practical applicability.

Temporal modulation strategies provide another pathway for dynamic color tuning. By varying the excitation pulse width or frequency, specific energy transfer channels can be selectively activated, leading to distinct color outputs. For example, pulsed 980 nm excitation with variable widths and frequencies has been shown to produce tunable green and red emissions,[26] and Kibrisli *et al.*[27] further demonstrated orange-green-white transitions using a pulsed 980 nm source. A seminal demonstration of this concept was reported by Deng *et al.*,[1] showing that full-color tuning could be achieved in upconversion nanocrystals by controlling excitation pulse width. More recently, Huang *et al.*[28] achieved RGB emission tuning under single-wavelength excitation using multi-shell nanoparticles combined with time-gated detection. While these approaches demonstrate powerful control over emission, they typically require additional equipment to regulate pulse width and frequency, complex multi-shell architectures, pulsed lasers, and sophisticated detection systems. These constraints increase setup complexity, hinder reproducibility, and limit integration into practical devices, underscoring the need for alternative strategies that enable tunable full-color upconversion using structurally simpler nanomaterials under continuous-wave excitation.

Power-density tuning represents a simpler, more cost-effective method for color tuning among external stimuli. By varying the excitation intensity, it is possible to selectively activate emission pathways at different photon orders. While some studies have achieved partial color tuning of Er^{3+} emissions, such as green-to-yellow or green-to-orange transitions, the absence of a pure red emission component has limited the color purity of these systems.[29–31] In 2018, Meng *et al.* achieved high-quality green and red emissions by adjusting 980 nm excitation power density.[32] However, adding Tm^{3+} to these systems typically results in white light emission due to color interference.[33] More recently, orthogonal RGB emission schemes have been proposed,[34] but these approaches require complex excitation geometries and still do not achieve full RGB tunability under a single excitation source.

To realize such tunability, $NaLnF_4$ (hexagonal-phase) was selected as the host lattice because its low phonon energy ($\sim$350 cm^{-1}) minimizes non-radiative relaxation, while its chemical stability and compatibility with multiple lanthanide dopants enable precise construction of core/shell/shell architectures with sharp interfaces and efficient energy transfer. Achieving RGB upconversion emissions with a single excitation wavelength would significantly simplify the operational complexity and setup costs of these luminescent nanocrystals for real-world applications. In this study, we present a breakthrough in developing structurally simple upconversion nanocrystals capable of emitting tunable RGB colors under a single excitation wavelength through a novel photon order dependent upconversion luminescence mechanism. A schematic illustration of the $NaYbF_4$:Er^{3+}@$NaYF_4$@$NaYF_4$:Yb^{3+},Tm^{3+} (C/S1/S2) nanoparticle design and power-dependent emission behavior is shown in Fig. 1. The RGB color components appear sequentially by simply adjusting the excitation power density. We explore the underlying mechanisms governing this RGB tunability. This novel upconversion nanocrystal simultaneously provides tunable RGB emissions, high color purity, compact structure and brightness, with promising applications in fields such as advanced high-resolution color display, anti-counterfeiting, multifunctional bio-probes, controlled drug release, and multi-spectral imaging. In a conventional display, each color is represented 2 $\times$ 2 pixels of [G, R; B, G] colors or color filters, and thus the resolution is determined by the total size of 2 $\times$ 2 pixels. However, this approach conceptually suggests that each nanocrystal could function as a full-color pixel under a single excitation source,[35] offering a possible route to higher display resolution compared to conventional RGB sub-pixel architectures. However, practical implementation would require additional developments in pixel-level control and device integration.

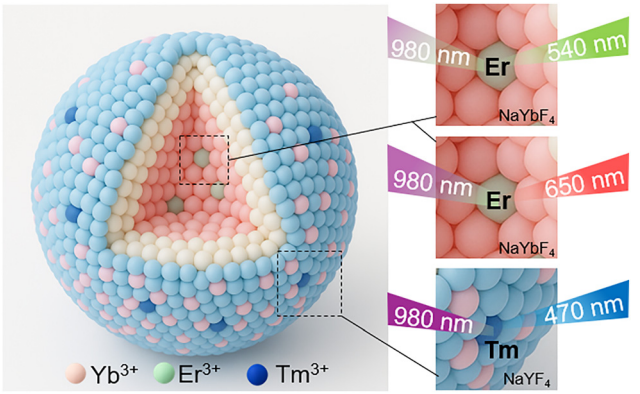

Fig. 1 Schematic of the core/shell/shell (C/S1/S2) nanocrystal with a $NaYF_4$:Er^{3+} core, inert $NaYF_4$ intermediate shell, and $NaYF_4$:Yb^{3+},Tm^{3+} outer shell, enabling power-dependent RGB emission tuning under CW 980 nm excitation.

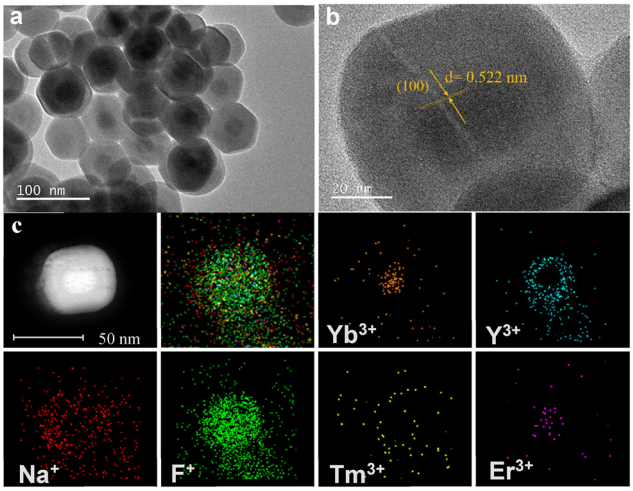

Fig. 2 (a) TEM image, (b) high-resolution TEM (HRTEM) of the as-synthesized luminescence color-tunable (C/S1/S2) nanocrystals. (c) High-angle annular dark-field (HAADF)-STEM images of a formed nanocrystal. The elemental mapping results confirm the distribution of ions within a single nanocrystal.

Results and discussion

In this work, we used hexagonal-phase $NaLnF_4$, a well-established upconversion host, to synthesize color-tunable nanocrystals.[36] The relatively straightforward (C/S1/S2) structure was synthesized, featuring rationally designed compositions of Er^{3+}/Yb^{3+} in the core and Tm^{3+}/Yb^{3+} in the outer shell (S2). An inert layer of pure $NaYF_4$ (S1) separates the two luminescent layers, effectively preventing cross-relaxation effects between Er^{3+} and Tm^{3+} after energy absorption during excitation. Yb^{3+} works as an efficient sensitizer, absorbing 980 nm NIR excitation and effectively transferring energy to Er^{3+} and Tm^{3+}, producing red/green and blue emissions, respectively. The TEM images in Fig. S1 indicate that the mean diameters of the nanospheres for the core only, core/shell (C/S1), and (C/S1/S2) nanocrystals are 25, 35, and 55 nm, respectively, with the incremental size increase confirming the successful growth of the encapsulation shells. The nanocrystals are well-dispersed (due to their small sizes) and exhibit high uniformity in both size and shape, indicating the absence of phase separation during epitaxial growth.

Fig. 2(a) also presents the TEM image of the synthesized (C/S1/S2) nanocrystals, which exhibit excellent monodispersed with uniform size and morphology, indicating well-controlled epitaxial growth without any observable phase separation. Fig. 1(b) displays the corresponding HRTEM image, where distinct lattice fringes with an interplanar spacing of 0.522 nm, assigned to the (100) plane of hexagonal-phase $NaLnF_4$, are clearly observed. This spacing is further supported by the HRTEM image shown in Fig. S2a. The fast Fourier transform (FFT) pattern in Fig. S2b confirms the high crystallinity of the nanocrystals. The inverse FFT (iFFT) image in Fig. S2c reveals well-resolved lattice fringes. At the same time, the corresponding intensity profile in Fig. S2d demonstrates periodic structural features, further validating the precision and structural order of the (C/S1/S2) architecture.

Fig. 2(c) presents the elemental mapping of a single (C/S1/S2) nanocrystal, highlighting the spatial distribution of Ln^{3+} across the core, intermediate shell, and outer shell. The distinct segregation of Yb^{3+}, Y^{3+}, Na^{+}, F^{+}, Tm^{3+} and Er^{3+} confirms the successful construction of the designed core–shell–shell architecture, essential for achieving tunable upconversion luminescence. In addition, photographs of the colloidal dispersions (Fig. S3) show that the solutions remain transparent and stable without precipitation, further confirming their good dispersion. The elemental composition of the synthesized (C/S1/S2) nanocrystal was further verified by energy-dispersive X-ray spectroscopy (EDS), as shown in Fig. S4. The phase purity of the synthesized nanocrystals was confirmed through powder X-ray diffraction (XRD) analysis as shown in Fig. S5. The XRD patterns of the synthesized nanocrystals confirm the formation of the pure hexagonal $NaYbF_4$:Er structure, which is crucial for efficient upconversion luminescence. The core $NaYbF_4$:Er nanocrystals exhibit sharp and well-defined diffraction peaks, consistent with the standard hexagonal-$NaYbF_4$ phase (JCPDS no. 27-1427). Upon growing the $NaYF_4$ inert shell, the XRD peaks remain unchanged, indicating the preservation of the hexagonal phase and successful epitaxial shell growth. Further coating with the $NaYF_4$:Yb^{3+},Tm^{3+} layer to form the (C/S1/S2) structure ($NaYbF_4$:Er^{3+}@$NaYF_4$@$NaYF_4$:Yb^{3+},Tm^{3+}) shows no additional diffraction peaks, indicating that the shell layers are crystalline and structurally coherent with the underlying core. The consistent diffraction peak positions and intensities across the core, core/shell, and core/shell/shell samples validate the integrity of the hexagonal phase throughout the hierarchical structure. While the overall particle size increases with additional shells, this primarily serves to suppress surface quenching and enhance brightness. The sequential green → red → blue color evolution is instead dictated by photon-order thresholds and dopant zoning, and is not directly dependent on the absolute particle size.

The upconversion luminescent spectra of the synthesized (C/S1/S2) nanocrystals are shown in Fig. 3. The excitation power

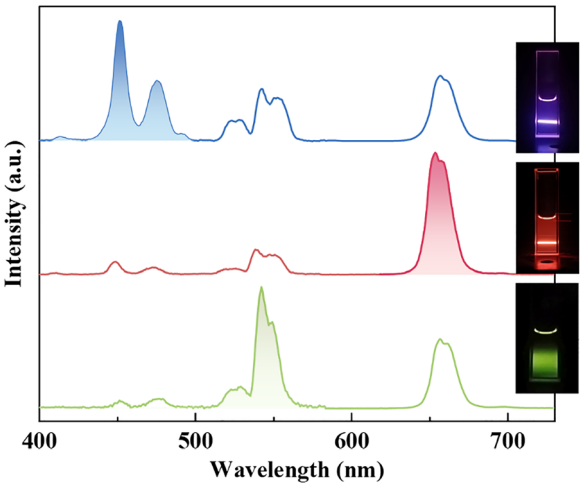

Fig.3

Fig. 3 Emission spectra of (C/S1/S2) nanocrystals measured under 980 nm excitation at weak (~1 W cm^{-2}), medium (~10 W cm^{-2}), and strong (~100 W cm^{-2}) power densities. The schematic representation on the left depicts the luminescence emitted by the colloidal nanocrystals at these excitation levels, emphasizing the color variations of each emission component. Luminescent images were captured using an Honor X50i+ cellphone, and to prevent signal blooming in the CMOS sensor, attenuation filters were applied for the red (10% transmittance) and blue (2.5% transmittance) emission images.

density was controlled by adjusting the output power of the 980 nm laser. Under weak excitation (~1 W cm^{-2}) conditions, the nanocrystals predominantly emit green luminescence with peaks at 525 and 540 nm, attributed to the $^2H_{11/2} \rightarrow {}^4I_{15/2}$ and $^4S_{3/2} \rightarrow {}^4I_{15/2}$ electronic transitions of Er^{3+}, respectively.

As the excitation power density increases (~10 W cm^{-2}), a notable and gradual shift in the dominant emission color occurs, transitioning first to red and subsequently to blue (~100 W cm^{-2}). The red emission peak at 650 nm arises from the $^4F_{9/2} \rightarrow {}^4I_{15/2}$ transition of Er^{3+}, while the blue emission peaks at 450 and 475 nm are attributed to the $^1D_2 \rightarrow {}^3F_4$ and $^1G_4 \rightarrow {}^3H_6$ transitions of Tm^{3+}, respectively.

This gradual color tuning is further quantified by examining the relative emission intensity ratios across different excitation power densities. With weak excitation, the integrated density ratio of green to red emission is 1.6, and that of green toon blue is 8, indicating a dominant green emission. When the excitation power density is increased to a moderate level, the integrated density ratio of red to green rises to 4.4, and red to blue increases to 10.7, demonstrating a shift towards red dominance. At high excitation power density, the integrated density ratios of blue to green and blue to red are both 1.6, confirming the emergence of a strong blue emission component. These findings demonstrate the effectiveness of the (C/S1/S2) nanocrystal system in achieving precise RGB color tuning using a single CW 980 nm excitation source. This tunable emission behavior highlights the potential of these nanocrystals for applications that require precise color control and high emission purity across the entire RGB spectrum. These ensemble measurements reflect the collective behavior of the nanocrystals, with the observed three-color emission arising from the intrinsic properties of the core/shell/shell structure.

Theoretically, the presence of activators Er^{3+} and Tm^{3+}, along with the sensitizer Yb^{3+}, allows the formed nanocrystals to emit red (Er^{3+}), green (Er^{3+}), and blue (Tm^{3+}) light under 980 nm excitation. However, achieving all RGB components simultaneously and controllably at varying excitation power densities poses a significant challenge. High-order upconversion emissions typically require the involvement of a greater number of excitation photons. Consequently, emissions originating from higher-lying electronic energy levels demand relatively high excitation thresholds. Increasing the excitation power density tends to enhance the emission intensity of high-lying energy levels more significantly than that of low-lying energy levels. Considering the energy hierarchy of the red and green emissions from Er^{3+} and the blue emission from Tm^{3+}, where these emissions arise from progressively higher energy levels, this property can be exploited to achieve tunable RGB emission using a single CW excitation source.

A major obstacle in this approach is that the green and red emissions from Er^{3+} are both primarily associated with two-photon absorption processes, that is the same photon order generates them. As a result, isolating pure green and red components is challenging by simply adjusting the excitation power density of a 980 nm laser in traditional Er^{3+}–Yb^{3+} co-doped materials, which are commonly employed for efficient visible upconversion emissions. To overcome the challenge of tunable green and red emissions, we selected a low-$Er^{3+}$and high Yb^{3+} doping composition of 2%Er^{3+} and 98%Yb^{3+}. As shown in Fig. 4, successive energy transfer (ET) processes from Yb^{3+} to Er^{3+}, coupled with rapid nonradiative relaxation, populate the Er^{3+} $^2H_{11/2}$ and $^4S_{3/2}$ levels, which are responsible for green emissions. This population pathway resembles the $NaYF_4$:Er^{3+}, Yb^{3+} (with 2% Er^{3+} and 18% Yb^{3+}) nanocrystals traditionally used for efficient green upconversion emission and corresponds to a two-photon upconversion process.[37]

When the excitation power density is further increased, electrons in the $^4S_{3/2}$ level are promoted to the higher-lying $^4G_{11/2}$ level. Following rapid relaxation to the $^2H_{9/2}$level, the Er^{3+} $^4F_{9/2}$ level, which is responsible for red emission, is populated *via* a back-energy transfer (BET) process described by: $^2H_{9/2}(Er^{3+}) + {}^2F_{7/2}(Yb^{3+}) \rightarrow {}^4F_{9/2}(Er^{3+}) + {}^2F_{5/2}(Yb^{3+})$, leading to a three-photon upconversion pathway for red emission. The ultrahigh Yb^{3+} doping level in the synthesized nanocrystals ensures the efficiency of this BET process. This mechanism effectively increases the photon order required for Er^{3+} red emission, enabling clear differentiation between the upconversion mechanisms for red and green emissions. Consequently, tuning the green and red emissions by varying the excitation power density is possible.

As a result, three-photon red upconversion luminescence dominates the emission spectrum of the nanocrystals under medium excitation power density. Zhang *et al.* previously demonstrated the feasibility of three-photon pathways for red emission by directly populating the Er^{3+} $^4G_{11/2}$ level using

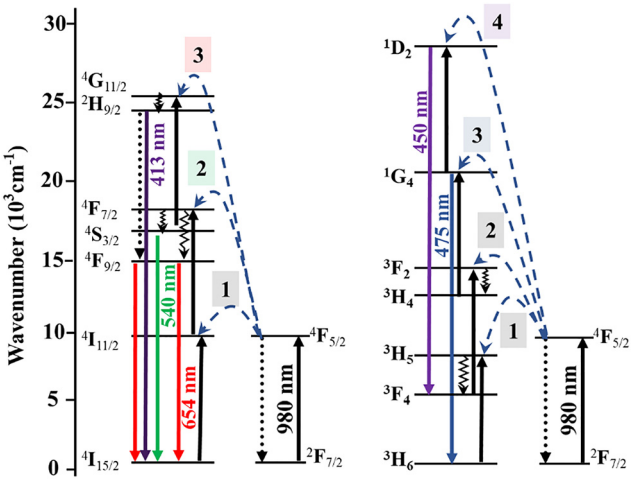

Fig. 4 Energy level diagrams of Er^{3+} and Tm^{3+} ions illustrating the upconversion pathways responsible for green (~540 nm), red (~654 nm), blue (~475 and 450 nm), and violet (~413 nm) emissions under 980 nm CW excitation. The labeled transitions correspond to two-, three-, and four-photon processes that enable sequential RGB tuning.

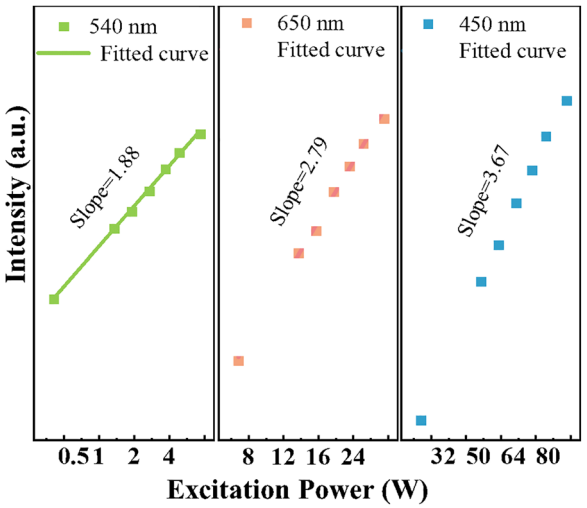

Fig. 5 Power-dependent upconversion emission intensities of green (540 nm, Er^{3+}), red (650 nm, Er^{3+}), and blue (450 nm, Tm^{3+}) channels under 980 nm excitation. Excitation power is displayed in watts (W) for clarity, with ranges of 0.5–8 W (green), 8–32 W (red), and 32–100 W (blue), corresponding to their respective dominance regimes. The slope values were extracted from ln–ln fitting of the data and confirm the two-photon (green), three-photon (red), and four-photon (blue) processes governing the sequential G → R → B color evolution.

378 nm excitation, resulting in bright red luminescence.[38] Further validation of the three-photon mechanism for red emission is provided by the appearance of a low-intensity emission band at 413 nm, as shown in Fig. S6, with a magnified view provided in the inset. This band, as previously reported, is characteristic of three-photon upconversion processes facilitated by Yb^{3+} sensitization, where energy transfer from Yb^{3+} ions enables sequential photon absorption, resulting in visible emission.[39] After achieving tunable red and green (R/G) emissions, a relatively high doping composition of $NaYF_4$:Yb^{3+},Tm^{3+} (with 2% Tm^{3+} and 18% Yb^{3+}) was selected for the outermost layer, following the growth of an inert $NaYF_4$ shell around the $NaYbF_4$:Er (with 2% Er) core.

The 475 nm and 450 nm emissions from Tm^{3+}, corresponding to the $^1G_4$ and $^1D_2$ levels, are associated with three- and four-photon upconversion processes. As the excitation power density increases, the faster growth of high-order upconversion intensities causes the fraction of the four-photon blue upconversion emission to gradually dominate the emission spectrum under strong excitation power. The photon-order dependence of the upconversion emission colors is directly supported by their corresponding power dependences. The slopes obtained from the logarithmic plots are 1.88 for the Er^{3+} green emission, 2.79 for the Er^{3+} red emission, and 3.67 for the Tm^{3+} blue emission, clearly validating the proposed two-, three-, and four-photon upconversion processes, respectively shown in Fig. 5. Time-resolved luminescence measurements further support this mechanistic interpretation in Fig. S7. The green emission (~540 nm, $^4S_{3/2} \rightarrow {}^4I_{15/2}$) exhibited relatively stable lifetimes (222–280 μs) across different power densities, whereas the red emission (~650 nm, $^4F_{9/2} \rightarrow {}^4I_{15/2}$) showed a moderate decrease (432 → 287 μs). The blue emission (~450 nm, $^1D_2 \rightarrow {}^3F_4$) displayed the strongest shortening (391 → 235 μs), consistent with its higher-order photon dependence. These lifetime results corroborate the power-dependent slopes, reinforcing that the sequential G → R → B evolution arises from distinct multiphoton pathways. Although the green emission remains visible across all excitation powers, its relative contribution systematically decreases as red and blue channels arising from higher-order processes grow more steeply with increasing power density. While these results establish the mechanistic basis of RGB tunability in our $NaLnF_4$-based nanocrystals, the same photon-order controlled strategy could, in principle, be extended to other low-phonon-energy hosts. The actual degree of tunability in different systems would likely depend on host stability, dopant solubility, and cross-relaxation dynamics. Thus, $NaLnF_4$ provides a particularly favorable platform, while exploration of other hosts remains an important direction for future studies.

In addition to the tunable green-to-red (G/R) emission achieved through the low-Er^{3+} and high-Yb^{3+} core composition, the fully tunable RGB color emission required a "switchable" blue emission. The suppression of blue emission ("off" state) was essential to avoid blending the blue component with the G/R emissions under weak to medium excitation power densities. In contrast, the enhancement of blue emission ("on" state) ensured its dominance over G/R emissions under strong excitation conditions. The relatively high doping concentrations of Tm^{3+} in the outermost S2 layer were critical for generating this switchable blue emission. Specifically, the Tm^{3+} concentration in the S2 layer was set at 2 mol%, which is 4 to 10 times higher than the traditionally optimal Tm^{3+} concentration (0.2–0.5 mol%) used for efficient blue emission.[40] This saturation, combined with the faster increase in blue emission intensity, contributed to the high purity of blue emission at

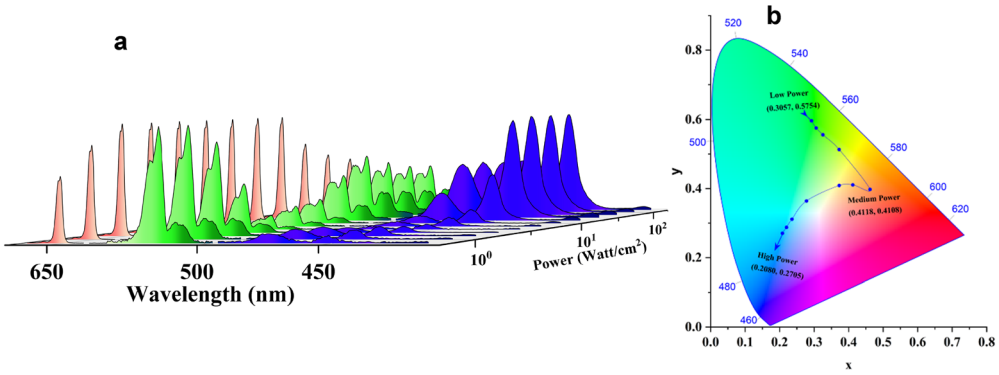

Fig. 6 (a) Power-dependent upconversion emission spectra of the color-tunable luminescence generated by the C-S1-S2 nanocrystals. (b) Corresponding CIE chromaticity coordinates illustrate the evolution of emission colors with increasing excitation power density.

strong excitation. Additionally, the increased intensity ratio under higher excitation power density is primarily due to the higher-order upconversion emissions (3-photon and 4-photon processes), which exhibit more pronounced intensity increases with rising power density.

Dynamic control over the upconversion emission color of nanocrystals was achieved by adjusting the excitation power density of a 980 nm laser. As the excitation power density increased from 1 to 100 W cm^{-2}, the dominant emission color exhibited a systematic shift from green to red, and finally to blue, corresponding to variations in the relative intensities of the RGB emission bands shown in Fig. 6.

The green emission band was the strongest at low excitation power density of 1 W cm^{-2}, while the red and blue bands were weak, as shown in Fig. 6(a). As the excitation power density increased, the intensity of the red emission band progressively strengthened, surpassing the green band, which became increasingly weaker. It is worth noting that the green emission band exhibits a comparatively lower intensity than the red and blue channels under 980 nm excitation. This behavior can be ascribed to the relatively inefficient population of the Er^{3+} $^4S_{3/2}$ level and the presence of cross-relaxation processes that preferentially enhance red emission. Despite this intensity imbalance, the green emission remains clearly distinguishable and enables a reliable representation of all three primary colors in the CIE chromaticity diagram, thereby maintaining the fidelity of the RGB tunability. At a medium power density of 10 W cm^{-2}, the red emission band dominated. Further increases in excitation power density led to a notable rise in the intensity of the blue emission band, which eventually became the strongest at a high-power density of 100 W cm^{-2}. Detailed emission spectra were recorded across varying excitation power densities to capture these transitions. The corresponding shifts in the chromaticity coordinates within the CIE diagram are shown in Fig. 6(b), confirming the observed color changes. The color point was in the green region at low excitation power densities. As the power density increased, the color point moved towards the longer wavelength region, with a dominant red emission observed at medium power densities. Upon further increases in excitation power density, the color point shifted into the blue region, ultimately stabilizing in the strong blue emission zone at the highest excitation powers. In Fig. 6(b), the representative chromaticity coordinates are labeled as (0.3057, 0.5754) for low power (green), (0.4118, 0.4108) for medium power (red), and (0.2080, 0.2705) for high power (blue). The corresponding color purity values were calculated to be 66% (green), 47% (red), and 48% (blue), confirming well-separated RGB states under power-dependent excitation. In addition to color purity, we evaluated the photoluminescence quantum yield (PLQY) of our nanocrystals, which reflects their radiative efficiency. Since the absorption cross-section was not directly measured, we use the PLQY as a comparative metric of emissive performance, acknowledging that absolute brightness is proportional to the product of the absorption cross-section and the PLQY. The PLQY of bare-core nanocrystals was consistent with reported literature values,[41] whereas our core/shell/shell structures exhibited significantly higher PLQYs, which can be attributed to optimized doping and inert shell passivation.[42,43] Moreover, the PLQY evolution with excitation power density (Fig. S8) revealed well-separated contributions from green, red, and blue channels, supporting the photon-order-dependent tuning mechanism and confirming enhanced brightness alongside distinct chromaticity. Owing to the limitations of the integrating sphere setup, PLQY measurements could not be obtained at the highest excitation powers. The laser beam spot size was measured to be $\sim$0.5 mm in diameter, and additional experimental details are available in our recent work.[44] A potential concern with high excitation power is local heating of the nanocrystal suspension. However, in our experiments, no visible degradation, color change, or burning of the samples was observed within the applied power density range ($\leq$100 W cm^{-2}). This indicates that heating effects were minimal under our conditions and did not influence the observed emission behavior. A summary of the results published in the literature on dynamic upconversion emission color tuning by manipulation of the 980 nm excitation power density is presented in Table S1. There, it can be seen that we achieved tunable full RGB upconversion emission color using a single CW laser excitation for the first time. Unlike conventional RGB systems, which require three separate excitation lasers, our compact core/shell/shell nanocrystals

achieve full RGB tunability with a single 980 nm source, while maintaining nanoscale size and brightness, underscoring their potential as a structurally simple and efficient alternative.

These findings highlight potential applications in scenarios where rapid estimation of power density is crucial. For instance, they could be employed to significantly improve the spatial resolution of a color display, and pre-check excitation dosages in phototherapy, helping to prevent overexposure. Furthermore, the nanocrystals can act as substrates for *in vitro* applications requiring precise power density indication. This study is particularly significant as it demonstrates, for the first time, tunable full RGB upconversion emission using a single CW laser excitation. This achievement underscores the potential for precise and dynamic color control in various advanced applications.

A balanced consideration of potential limitations is also important. Because power-dependent upconversion relies on nonlinear multiphoton processes, the emission can be highly sensitive to variations in excitation intensity, which may affect reproducibility under different experimental conditions. In our measurements, no degradation or burning was observed, suggesting that local heating was not significant within the applied power range ($\leqslant$100 W cm^{-2}). However, heating effects may become more relevant under higher power densities or in solid-state environments. In addition, particle-to-particle variability could lead to slight differences in emission balance across ensembles, which may influence scalability for large-area or device-level applications. These aspects should be considered in future studies aiming at practical implementation.

Conclusion

This study demonstrates an innovative approach to dynamically controlling the upconversion emission color of nanocrystals through precise modulation of the excitation power density of a single CW laser. With a designed compact core/shell/shell upconversion nanocrystal, we have achieved tunable RGB colors using a single CW laser at 980 nm. The unique compositions of 2%Er/98%Yb in the core and 2%Tm/18%Yb in the outermost layer enabled dominant green and red emissions at lower and moderate power densities, with switchable blue emission emerging under higher power densities. The photon-order-dependent upconversion processes played a critical role in modulating luminescence pathways, ensuring precise emission control without interference. These results not only provide deeper insights into the mechanisms of upconversion emission but also open new possibilities for practical applications. The ability to achieve tunable RGB emission with a simplified excitation setup has significant implications for fields such as high-resolution color display, power density sensing, phototherapy, optical storage, and advanced anti-counterfeiting. Multi-wavelength excitation strategies can also be employed for achieving hyperspectral or multispectral imaging[45] for *e.g.* biomedical applications. This single-source RGB strategy offers a practical route to reduce optical complexity relative to three-laser systems, while preserving nanoscale dimensions and strong, well-separated emissions. This work paves the way for enhancing the functionality and versatility of modern optical devices.

Experimental section

Materials

Rare-earth chlorides were procured from Aladdin, while sodium acetate, sodium hydroxide, and ammonium fluoride were obtained from SCR Chemicals (Pty) Ltd. The rare-earth oleates (RE-oleates) were synthesized following an established procedure, with some modifications.[46]

Synthesis of hexagonal phase $NaYbF_4$:2%Er

To synthesize hexagonal-phase $NaYF_4$:Er nanoparticles, 1 mmol of RE-oleates with a Yb : Er molar ratio of 0.98 : 0.02 was used. The RE-oleates were combined with 5 mL of 1-octadecene and 10 mL of oleic acid. This mixture was heated to 60 °C to evaporate the ethanol completely. Subsequently, the temperature was raised to 160 °C and maintained for 30 minutes under a steady flow of argon gas. Afterward, the solution was allowed to cool to room temperature, during which the residual gases were removed. Separately, 4 mmol of ammonium fluoride (NH_4F) and 2.5 mmol of sodium hydroxide (NaOH) were dissolved in 10 mL of methanol. This solution was added to the cooled reaction mixture in a three-necked flask. The combined solution was then heated to 300 °C at a controlled rate of 20 °C per minute and held at this temperature for 90 minutes. Following the reaction, the mixture was allowed to cool naturally to ambient temperature, leading to the precipitation of the product in acetone. The precipitate was collected *via* centrifugation, washed multiple times with ethanol to remove impurities, and centrifuged again. Finally, the purified samples were dispersed in hexane for storage and further analysis.

Synthesis of the shell for $NaYbF_4$:2%Er

The $NaYF_4$ shell was grown over the $NaYbF_4$:2%Er^{3+} core using a well-controlled thermal decomposition method. Initially, a precursor solution with a standard concentration of sodium, yttrium, and fluoride sources was prepared to serve as the shell material. The precursor solution was carefully mixed with the pre-synthesized $NaYbF_4$:2%Er^{3+} core nanoparticles, ensuring a homogeneous dispersion of the core particles within the reaction medium. This mixture was then transferred to a three-necked flask equipped with a condenser, thermometer, and argon gas inlet to maintain an inert atmosphere. The system was gradually heated to a temperature of 300 °C at a controlled rate to avoid sudden thermal shocks, which could compromise the quality of the shell growth. Once the reaction temperature reached 300 °C, it was maintained for 1.5 hours to enable the controlled deposition of the $NaYF_4$ shell onto the $NaYbF_4$:2%Er^{3+} core particles. During this period, the high temperature facilitated the thermal decomposition of the precursor solution, allowing the formation and uniform growth of the

$NaYF_4$ shell around the core nanoparticles. After the reaction, the system was allowed to cool naturally to room temperature. The resulting core–shell nanoparticles were precipitated by adding a suitable solvent, such as acetone or ethanol, and collected *via* centrifugation. To ensure the removal of unreacted precursors and by-products, the precipitate was washed several times with ethanol and centrifuged again. Finally, the purified core–shell nanoparticles were dispersed in hexane for storage and further characterization.

Synthesis of $NaYbF_4$:2%Er@$NaYF_4$@$NaYF_4$:18%Yb,2%Tm

The outer shell was grown over the $NaYbF_4$:2%Er@$NaYF_4$ core by heating a precursor solution containing standard concentrations of sodium, yttrium, and fluoride sources to 300 °C. The precursor solution was mixed with the pre-synthesized $NaYbF_4$:2%Er@$NaYF_4$ cores, ensuring even dispersion in the reaction medium. The mixture was maintained at 300 °C for 1.5 hours under an inert argon atmosphere, allowing the precursor to decompose and deposit the shell material uniformly over the core. After the reaction, the mixture was cooled to room temperature, and the resulting core–shell nanoparticles were collected through precipitation, washed thoroughly with ethanol, and finally dispersed in hexane for further use and characterization.

The dopant ratios (2% Er^{3+}/98% Yb^{3+} in the core and 2% Tm^{3+}/18% Yb^{3+} in the outer shell) were selected based on previous reports and optimized for sequential color tuning. The high Yb^{3+}/low Er^{3+} core enables efficient sensitization under 980 nm excitation while suppressing quenching, whereas the relatively high Tm^{3+} content in the shell was chosen to raise the activation threshold for blue emission, ensuring stepwise G → R → B transitions.

Sample characterization

Morphological analysis was conducted using high-resolution transmission electron microscopy (JEOL-2010) to determine the particle size and shape. Phase and structural identification were carried out through X-ray diffraction (XRD) using a Rigaku Smart Lab diffractometer with Cu-Kα radiation (wavelength: 0.154056 nm). Emission spectra were recorded on a fluorescence spectrometer (Princeton Instruments Acton SP 2750) equipped with a 980 nm laser as the excitation source. All optical measurements in this study were performed on ensembles of nanocrystals dispersed in solution. While individual nanocrystal behavior may vary slightly, the ensemble data reliably reflect the emission characteristics of the core/shell/shell structures. For quantitative analysis, the emission channels were integrated over fixed wavelength ranges: blue (440–480 nm, Tm^{3+}), green (520–560 nm, Er^{3+}), and red (640–670 nm, Er^{3+}). These intervals were used consistently for spectral integration, chromaticity calculations, and comparison of power-dependent emission behaviors.

Conflicts of interest

There are no conflicts to declare.

Data availability

The datasets supporting this article have been included in the main text and the supplementary information (SI). Supplementary information is available. See DOI: **https://doi.org/10.1039/d5mh01409c**.

Additional raw data or materials related to the findings of this study are available from the corresponding author upon reasonable request.

Acknowledgements

We would like to acknowledge the financial partial support from the ''Pioneer'' and ''Leading Goose'' R&D Program of Zhejiang Province (2025C02140, 2023C03083), the National Natural Science Foundation of China (W2412107, 91833303, 11621101), the Ningbo Science and Technology Project (No. 2024Z146, 2023Z179, 2021Z030), the National Key Research and Development Program of China (2022YFC3601003), and the Fundamental Research Funds for the Central Universities (3072024LJ2503). The Special Development Fund of Shanghai Zhangjiang Science City. The authors are grateful to Drs Jing Ren and Jianzhong Zhang of Harbin Engineering University and Dr Julian Evans of Zhejiang University for valuable discussions.

References

1 R. Deng, F. Qin, R. Chen, W. Huang, M. Hong and X. Liu, *Nat. Nanotechnol.*, 2015, **10**, 237–242.
2 P. Zijlstra, J. W. M. Chon and M. Gu, *Nature*, 2009, **459**, 410–413.
3 M. You, J. Zhong, Y. Hong, Z. Duan, M. Lin and F. Xu, *Nanoscale*, 2015, **7**, 4423–4431.
4 Y. Chen, Y. Zheng, J. Wang, X. Zhao, G. Liu, Y. Lin, Y. Yang, L. Wang, Z. Tang, Y. Wang, Y. Fang, W. Zhang and X. Zhu, *Sci. Adv.*, 2024, **10**(23), eadm9631.
5 C.-J. Shih, Y.-C. Huang, T.-Y. Wang, C.-W. Yu, I.-S. Hsu, A. K. Akbar, J.-Y. Lin, S. Biring, J.-H. Lee and S.-W. Liu, *Sci. Adv.*, 2023, **9**(17), eadd7526.
6 H.-X. Mai, Y.-W. Zhang, L.-D. Sun and C.-H. Yan, *J. Phys. Chem. C*, 2007, **111**, 13721–13729.
7 W. Gao, H. Zheng, Q. Han, E. He, F. Gao and R. Wang, *J. Mater. Chem. C*, 2014, **2**, 5327–5334.
8 G. K. Das, D. T. Stark and I. M. Kennedy, *Langmuir*, 2014, **30**, 8167–8176.
9 D. Hudry, D. Busko, R. Popescu, D. Gerthsen, I. A. Howard and B. S. Richards, *J. Mater. Chem. C*, 2019, **7**, 7371–7377.
10 L. Xu, J. Li, K. Lu, S. Wen, H. Chen, M. K. Shahzad, E. Zhao, H. Li, J. Ren, J. Zhang and L. Liu, *ACS Appl. Nano Mater.*, 2020, **3**, 2517–2526.
11 S. Chen, A. Z. Weitemier, X. Zeng, L. He, X. Wang, Y. Tao, A. J. Y. Huang, Y. Hashimotodani, M. Kano, H. Iwasaki, L. K. Parajuli, S. Okabe, D. B. L. Teh, A. H. All, I. Tsutsui-Kimura, K. F. Tanaka, X. Liu and T. J. McHugh, *Science*, 2018, **359**, 679–684.

12 K. Lu, X. Sun, L. Xu, B. Jiang, J. Ren, J. J. Carvajal, E. Zhao, L. Liu and J. Zhang, *J. Alloys Compd.*, 2020, **842**, 155602.
13 S. Chen, *Science*, 2019, **365**, 456–457.
14 Y. Yang, Q. Shao, R. Deng, C. Wang, X. Teng, K. Cheng, Z. Cheng, L. Huang, Z. Liu, X. Liu and B. Xing, *Angew. Chem., Int. Ed.*, 2012, **51**, 3125–3129.
15 C. Renero-Lecuna, R. Martín-Rodríguez, R. Valiente, J. González, F. Rodríguez, K. W. Krämer and H. U. Güdel, *Chem. Mater.*, 2011, **23**, 3442–3448.
16 Y. Liu, D. Wang, J. Shi, Q. Peng and Y. Li, *Angew. Chem., Int. Ed.*, 2013, **52**, 4366–4369.
17 S. Guo, X. Xie, L. Huang and W. Huang, *ACS Appl. Mater. Interfaces*, 2016, **8**, 847–853.
18 P. Du, L. Luo and J. S. Yu, *Part. Part. Syst. Charact.*, 2018, **35**(3), 1700416.
19 R. A. Janjua, U. Farooq, R. Dai, Z. Wang and Z. Zhang, *Opt. Lett.*, 2019, **44**, 4678.
20 E. Downing, L. Hesselink, J. Ralston and R. Macfarlane, *Science*, 1996, **273**, 1185–1189.
21 X. Li, Z. Guo, T. Zhao, Y. Lu, L. Zhou, D. Zhao and F. Zhang, *Angew. Chem., Int. Ed.*, 2016, **55**, 2464–2469.
22 M. Wu, L. Yan, T. Wang, B. Zhou and Q. Zhang, *Adv. Funct. Mater.*, 2019, **29**(25), 1804160.
23 Z. Lei, X. Ling, Q. Mei, S. Fu, J. Zhang and Y. Zhang, *Adv. Mater.*, 2020, **32**(9), 1906225.
24 A.-R. Hong, J.-H. Kyhm, G. Kang and H. S. Jang, *Nano Lett.*, 2021, **21**, 4838–4844.
25 Z. Zhou, Y. Liu, X. Sun, L. Xu, F. Khan, Y. Li, L. Li, H. Li, J. Ren, J. Zhang and L. Liu, *Opt. Lett.*, 2021, **46**, 900.
26 Y. Han, H. Li, Y. Wang, Y. Pan, L. Huang, F. Song and W. Huang, *Sci. Rep.*, 2017, **7**, 1320.
27 O. Kıbrıslı, N. Vahedigharehchopogh, A. E. Ersundu and M. Çelikbilek Ersundu, *J. Phys. Chem. C*, 2020, **124**, 10687–10695.
28 J. Huang, L. Tao, H. Wei, H. Huang, Q. Zhang and B. Zhou, *Nat. Commun.*, 2025, **16**, 2378.
29 B. P. Singh, A. K. Parchur, R. K. Singh, A. A. Ansari, P. Singh and S. B. Rai, *Phys. Chem. Chem. Phys.*, 2013, **15**, 3480.
30 A. Zhou, F. Song, Y. Han, F. Song, D. Ju, K. Adnan, L. Liu and M. Feng, *J. Lumin.*, 2018, **194**, 225–230.
31 D. Gao, X. Zhang, B. Chong, G. Xiao and D. Tian, *Phys. Chem. Chem. Phys.*, 2017, **19**, 4288–4296.
32 Z. Meng, S. Wu and S. Zhang, *J. Mater. Chem. C*, 2018, **6**, 13101–13107.
33 Z. Meng, S. Zhang and S. Wu, *J. Lumin.*, 2020, **227**, 117566.
34 F. Farooq, S. Shin, J. Y. Lee, J. Kyhm, G. Kang, H. Ko and H. S. Jang, *ACS Appl. Mater. Interfaces*, 2024, **16**, 38221–38230.
35 T. Guo, Z. Zhang, Z. Lin, J. Tian, Y. Jin, J. Evans, Y. Xu and S. He, *Nat. Nanotechnol.*, 2024, **19**, 1635–1643.
36 R. A. Janjua, C. Gao, R. Dai, Z. Sui, M. A. Ahmad Raja, Z. Wang, X. Zhen and Z. Zhang, *J. Phys. Chem. C*, 2018, **122**, 23242–23250.
37 X. Zhu, W. Feng, J. Chang, Y.-W. Tan, J. Li, M. Chen, Y. Sun and F. Li, *Nat. Commun.*, 2016, **7**, 10437.
38 X. Zhang, Z. Zhang, Z. Liu, C. Zhang, B. Zhang, X. Mi and H. Zheng, *J. Lumin.*, 2019, **205**, 374–379.
39 X. Sang, W. Chen, P. Chen, X. Liu and J. Qiu, *J. Mater. Chem. C*, 2015, **3**, 9089–9094.
40 J. Zhao, D. Jin, E. P. Schartner, Y. Lu, Y. Liu, A. V. Zvyagin, L. Zhang, J. M. Dawes, P. Xi, J. A. Piper, E. M. Goldys and T. M. Monro, *Nat. Nanotechnol.*, 2013, **8**, 729–734.
41 J.-C. Boyer and F. C. J. M. van Veggel, *Nanoscale*, 2010, **2**, 1417.
42 D. Liu, X. Xu, F. Wang, J. Zhou, C. Mi, L. Zhang, Y. Lu, C. Ma, E. Goldys, J. Lin and D. Jin, *J. Mater. Chem. C*, 2016, **4**, 9227–9234.
43 X. Xu, Z. Zhou, Y. Liu, S. Wen, Z. Guo, L. Gao and F. Wang, *APL Photonics*, 2019, **4**, 026104.
44 X. Wang, R. Wang, Y. Jin, J. Liu, Y. Chu, Y. Tian, J. Ren, L. Liu and J. Zhang, *J. Mater. Chem. C*, 2025, **13**, 13890–13899.
45 Y. Zeng, X. Wang, L. Jiang, J. Qi, Z. Lin, T. Guo and S. He, *Opt. Lett.*, 2025, **50**(19), 6177–6180.
46 R. A. Janjua, O. Iqbal, M. A. Ahmed, A. A. Al-Kahtani, S. Saeed, M. Imran and A. G. Wattoo, *RSC Adv.*, 2021, **11**, 20746–20751.